Research article

Role of Si segregation in the structural, mechanical, and compositional evolution of high-temperature oxidation resistant Cr-Si-B$_{2\pm z}$ thin films

L. Zauner [a],[*],[1], A. Steiner [a], T. Glechner [a], A. Bahr [a], B. Ott [b], R. Hahn [a], T. Wojcik [a,c], O. Hunold [d], J. Ramm [d], S. Kolozsvári [e], P. Polcik [e], P. Felfer [b], H. Riedl [a,c]

[a] Christian Doppler Laboratory for Surface Engineering of high-performance Components, TU Wien, Austria
[b] Department of Materials Science, Friedrich-Alexander-Universität Erlangen-Nürnberg, Germany
[c] Institute of Materials Science and Technology, TU Wien, Austria
[d] Oerlikon Balzers, Oerlikon Surface Solutions AG, Liechtenstein
[e] Plansee Composite Materials GmbH, Germany

A B S T R A C T

This work investigates the influence of Si-alloying up to 17 at.% on the structural, mechanical, and oxidation properties of magnetron sputtered CrB$_{2\pm z}$-based thin films. Density-functional theory calculations combined with atom probe tomography reveal the preferred Si occupation of Cr-lattice sites and an effective solubility limit between 3 to 4 at.% in AlB$_2$-structured solid solutions. The addition of Si results in refinement of the columnar morphology, accompanied by enhanced segregation of excess Si along grain boundaries. The microstructural separation leads to a decrease in both film hardness and Young's modulus from $H \sim 24$ to 17 GPa and $E \sim 300$ to 240 GPa, respectively, dominated by the inferior mechanical properties of the intergranular Si-rich regions. Dynamic thermogravimetry up to 1400 °C reveals a significant increase in oxidation onset temperature from 600 to 1100 °C above a Si content of 8 at.%. In-situ X-ray diffraction correlates the protective mechanism with thermally activated precipitation of Si from the Cr-Si-B$_{2\pm z}$ solid solution at 600 °C, enabling the formation of a stable, nanometer-sized SiO$_2$-based scale. Moreover, high-resolution TEM analysis exposes the scale architecture after dynamic oxidation to 1200 °C (10 K/min heating rate) – consisting only of ~20 nm amorphous SiO$_2$ beneath ~200 nm of nanocrystalline Cr$_2$O$_3$. In summary, the study provides detailed guidelines connecting the chemical composition with the respective thin film properties of high-temperature oxidation resistant Cr-Si-B$_{2\pm z}$ coatings.

1. Introduction

Transition metal diboride (TMB$_2$) thin films are promising candidates to replace state-of-the-art functional and protective coating materials in a wide range of applications [1–8]. TMB$_2$s typically feature a high melting temperature, excellent thermal stability, as well as high hardness and strength, thus providing a strong incentive for ultra-high temperature applications [9–13]. However, this outstanding property spectrum is usually confined to inert atmospheres due to the consecutive/competitive formation of both TM- and B-based oxide scales, both usually incapable of forming a fully protective layer at temperatures beyond 600–700 °C [14–18]. More

drastically, above ~1100 °C linear mass gain kinetics are regularly observed, which coincides with the evaporation of the glassy-like boria (B$_2$O$_3$) embedded within the non-protective, porous metal oxide [18,19].

Different alloying concepts have been studied and implemented successfully to address the poor oxidation resistance of TMB$_2$ bulk and thin film materials. Adding Si-containing compounds such as SiC, MoSi$_2$, Si$_3$N$_4$, or Ta$_5$Si$_3$ is the most commonly used method for bulk diboride materials and improves the oxidation resistance by forming a stable, amorphous (boro-)silicate surface layer [19–21]. For instance, Fahrenholtz et al. demonstrated that adding SiC to ZrB$_2$ and HfB$_2$ permits drastically decreased oxidation rates up to 1600 °C [19].

Regarding TMB$_2$-based thin film materials, several ternary alloying routes, e.g., the addition of Al(B$_2$), TaB$_2$, or CrB$_2$, have been explored to improve the oxidation resistance [14–16,22,23]. Bakhit et al. [15] demonstrated that Al alloying into TiB$_2$-based thin films

* Correspondence to: Christian Doppler Laboratory for Surface Engineering of high-performance Components, TU Wien, Getreidemarkt 9, 1060 Wien, Austria.
E-mail address: lukas.zauner@tuwien.ac.at (L. Zauner).
[1] **ORCID-ID:** 0000–0002-8373–6552

significantly retards the oxide scale growth at temperatures up to 800 °C based on the formation of a dense Al-oxide surface layer. Moreover, Kashani et al. [17] showed that the Ti-Al-B$_{2 \pm z}$ system even outperforms the corresponding nitride system at 700 °C, especially for stoichiometric compositions close to B/TM ratios of 2. Indeed, this necessity for tailoring the B/TM-ratio within TiB$_{2 \pm z}$ thin films to optimize oxidation properties is highlighted in several works and rationalized by the fast-track oxidation pathway created through excess B-rich phases preferentially located at column and grain boundaries [24–26]. However, this effect appears specific to the material system and/or annealing treatment conditions, since a stable, protective boria surface layer was observed for HfB$_{2.3}$ thin films up to 900 °C [27].

A seemingly universal alloying route for improved oxidation resistance was recently published by Glechner et al. [28,29], showing that co-sputtering of pure Si to various TMB$_2$ (TM = Ti, Cr, Hf, Ta, W) drastically improves the oxidation resistance in all materials, with the onset of oxidation elevated to 1200 °C specifically for Cr-Si-B$_2$ and Hf-Si-B$_2$. Thereby, the protective mechanism relies on the formation of a stable Si-rich oxide scale above the formed TM-Si-B$_2$ solid solution.

Inevitably, the ensemble of available tools to improve the oxidation resistance within TMB$_2$ thin films influences the property spectrum of the initial binary alloy. While strategies involving ternary TM$_1$-TM$_2$-B$_{2 \pm z}$ thin films proved successful only below 800 °C, their mechanical properties, including hardness and fracture toughness, can often be preserved or even improved over the corresponding binary constituents [13–15]. Contrary, Si-based protective mechanisms can result in superior high-temperature performance of TM-Si-B$_2$ thin films, however, typically at the expense of reduced mechanical properties at higher Si contents [28,30]. Consequently, finding the optimum alloying content to achieve the desired oxidation resistance while maintaining good mechanical properties is a vital prerequisite for an industrial application of the entire TM-Si-B$_2$ material family.

Therefore, within this work we systematically study the influence of Si-alloying on the structural evolution, phase stability, as well as the mechanical and oxidation properties of magnetron sputtered Cr-Si-B$_{2 \pm z}$ thin films. This novel high-temperature ceramic is modelled by density functional theory calculations to reveal the energetically preferred lattice occupation of the alloying atom within various AlB$_2$-structured compositions. Furthermore, limitations in the accessible alloying range to yield solid solutions are discussed in conjunction with detailed atom probe tomography, thereby spanning a clear connection to the observed thin film growth and mechanical properties. The mechanism leading to the drastically increased oxidation resistance is revisited through dynamic oxidation, in-situ X-ray diffraction, and transmission electron microscopy, thus providing an in-depth correlation to the thin film properties towards finding an optimum Si alloying composition.

2. Experimental

Cr-Si-B$_{2 \pm z}$ thin films were synthesized from a 3-inch CrB$_2$ target (Plansee Composite Materials GmbH, 99.3% purity) in a pure Ar atmosphere (99.999% purity) using direct current magnetron sputtering in an in-house developed deposition system (base pressure below 1.0×10^{-4} Pa). The Si content was adjusted by placing 0, 2, 4, 6, 8, 12, or 16 Si platelets (3.5 × 3.5 × 0.38 mm) on the target racetrack. The rotating substrate holder (0.25 Hz) was positioned at a target-to-substrate distance of 90 mm. All thin films were grown on Si ((100)-oriented, 20 × 7 × 0.38 mm), single crystalline Al$_2$O$_3$ ((1−102)-oriented, 10 × 10 × 0.53 mm), and poly-crystalline Al$_2$O$_3$ (20 × 7 × 0.38 mm) substrates, which were ultrasonically pre-cleaned in acetone and isopropanol, respectively. Following a heating sequence to a substrate temperature of 550 °C, an Ar-ion etching step was performed at a total

pressure of 5 Pa and an applied substrate bias potential of −800 V for 10 min. The target and Si alloying platelets were sputter-cleaned for 3 min prior to all depositions to reduce oxygen contamination. The thin films were then grown at a total Ar pressure of 0.7 Pa, a target current of 0.4 A (corresponds to a power density of ~5 W/cm²), and a bias potential of −40 V. The synthesis conditions resulted in deposition rates of 16.1 and 18.1 nm/min for 0 and 16 Si platelets on the target surface. Aiming for a consistent coating thickness of ~3 μm, deposition times of 190 and 170 min were selected, respectively. Deposition times for intermediate Si compositions were calculated from linear interpolation, resulting in a total thickness variation of ± 0.1 μm between all samples.

The overall chemistry of the Cr-Si-B$_{2 \pm z}$ coatings was obtained using liquid inductively coupled plasma-optical emission spectroscopy (ICP-OES). A detailed explanation of this methodology is given in Ref. [28]. Structural analysis was performed by X-ray diffraction on a PANalytical XPert Pro MPD equipped with a Cu-K$_\alpha$ radiation source (wave-length λ = 1.54 Å, operated at 45 kV and 40 mA) in Bragg-Brentano geometry. The cross-sectional growth morphology was further investigated by scanning-electron microscopy (ZEISS Sigma 500VP, operated at 5 kV) on coated Si substrates.

The hardness and elastic modulus of all coatings was studied using instrumented nanoindentation (ultra-micro indentation system, UMIS) with a minimum of 30 load-displacement curves evaluated according to Ref. [31] for each coating. Increasing indentation loads ranging from 5 to 22 mN (steps of 0.5 mN), with additional measurements up to 45 mN to probe for any substrate influence, were applied. Moreover, the obtained E values were fitted over the indentation depth using a power law function and extrapolated to the sample surface to receive the film-only modulus [32]. Macro-stresses in the coatings were additionally analyzed through curvature measurements using optical profilometry (PS50, Nanovea) and the modified Stoney equation [33,34]. All mechanical properties were determined on coated sapphire substrates.

The oxidation behavior of the Cr-Si-B$_{2 \pm z}$ thin films was determined from thermogravimetric analysis (TGA, Netzsch STA 449 F1, equipped with a Rhodium furnace) performed on coated polycrystalline Al$_2$O$_3$ substrates. The substrates were weighed before and after deposition to determine the coating-only mass. This value serves as a reference during dynamic oxidation experiments up to 1400 °C (heating rate of 10 °C/min) in a synthetic air environment (50 ml/min flow rate). Any oxidation-related mass change was recorded at a resolution of 0.1 μg. Pre-tests on uncoated Al$_2$O$_3$ substrates additionally proved their inertness during the oxidation treatment [28].

Additional oxidation experiments combined with in-situ X-ray diffraction analysis were carried out on a PANalytical XPert Pro MPD (Cu-K$_\alpha$ radiation source, wave-length λ = 1.54 Å, operated at 45 kV and 40 mA) in Bragg-Brentano geometry using an Anton Paar high-temperature furnace chamber (HTK 1200 N). Measurements were taken in a lab-air environment (0.3 l/min flow rate) at room-temperature and from 400 to 1200 °C in 50 °C steps. The sample was heated at a rate of 50 °C/min between the individual temperature steps, with each diffraction measurement taking ~21 min

Furthermore, detailed microstructural and chemical analysis on selected oxidized samples was performed using transmission electron microscopy (TEM, FEI TECNAI F20, operated at 200 kV). Bright-field (BF) and high-angle annular dark field (HAADF) imaging are utilized to gain information on the microstructure and oxide scale growth. In addition, energy dispersive X-ray spectroscopy (EDX) performed in scanning TEM (STEM) revealed the chemical composition of the entire coating cross-section as well as the oxide layer.

Density functional theory (DFT) coded VASP [35,36] calculations (projector augmented waves method within the generalized gradient approximation [37]) were performed to study the preferred atomic configuration for silicon alloying atoms within various AlB$_2$-structured Cr-Si-B$_2$ compositions. Moreover, the influence of

increasing Si content as well as the impact of various vacancy configurations on the phase stability were investigated. The influence of vacancies was studied up to a content of 2 Si atoms within the supercell (corresponds to ~4 at.%), with 2 vacancies introduced either on the Cr-sublattice, the B-sublattice, or as a Schottky defect. All 2 × 2 × 4 supercell structures (16 metal and 32 boron atoms) were generated using the special quasi-random structure (SQS) approach [38]. Values for the formation energy were only extracted from fully converged supercells. A plane wave cut-off energy of 600 eV and an automated k-point mesh (length = 60) were chosen to provide a total energy accuracy of about 10^{-3} eV/at. All calculations were conducted without considering the paramagnetic states of Cr.

Finally, atom probe tomography (APT) analysis was performed on an exemplary coating in the as-deposited state to reveal the initial elemental distribution. Sample preparation involved milling of an initial coating pillar and sharpening to a tip using a focused ion beam microscope FEI Scios 2 DualBeam operated at 30 kV and stepwise decreasing milling currents. Final tip sharpening was performed at 50 pA, with a subsequent clean-up step at 5 kV and 28 pA to minimize possible Ga^+ ion-induced damage. Subsequent APT analysis was carried out on a CAMECA LEAP 4000X HR in pulsed laser mode with a set pulse energy of 50 pJ. The system uses a 355 nm UV laser equipped with a reflection lens, resulting in a detection efficiency of ~37%. The sample was cooled to a constant temperature of 44 K. Experiments were performed with a target evaporation rate of 1% and pulse repetition rate of 200 kHz. Data analysis was conducted using an open-source Matlab Toolbox for APT data evaluation [39].

3. Results & discussion

3.1. Computational phase formation & stability boundaries

A regular requirement for alloying strategies to successfully improve the oxidation resistance of a coating material involves unaltered phase stability for the host structure to maintain a distinct property profile. This necessity is demonstrated by the well-studied $Ti_{1-x}Al_xN$ system, where the oxidation resistance of rock-salt structured TiN scales with the AlN alloying fraction [40]. However, upon exceeding the Al solubility threshold on the metal sublattice ($x \sim$ 67% for DCMS deposited thin films), precipitation of the thermodynamically favored wurtzite-structured $Al_{1-x}Ti_xN$ phase occurs, thus deteriorating both the thermal stability and mechanical properties. Analogously, to probe the effect of an increasing Si alloying content on the phase stability of prototypical Cr-Si-B_2 thin films from a theoretical point of view, Fig. 1a presents ab initio calculated formation energies for various AlB_2 structured compositions. This evaluation allows to assess the influence of Si-addition on the phase stability but also provides information on the energetically preferred lattice occupation within the unit cell and hence a guideline for the Si solubility limit.

The model assumes that up to 8 Si atoms are either placed interstitially or substitutionally within the AlB_2-structured Cr-Si-B_2. Over the entire compositional range, DFT calculations associate the formation of all possible alloying configurations with an increasing E_f compared to the binary CrB_2 composition. This implies an overall reduced stability of the hexagonal structure with increasing Si content. In more detail, all structures where Si is placed interstitially either within B- or Cr-planes show the most substantial increase in E_f, already leading to positive formation energies upon alloying 2 Si atoms (equals ~4 at.%). Hence, these structures are energetically unstable, and all substitutional configurations are significantly more favored.

The structures where Si is placed in substitution for B/ Cr/ or equally on both sublattices exhibit very similar formation energies in the low alloying regime and thus can co-exist without any preferred atomic position of Si. However, upon increasing the alloying content
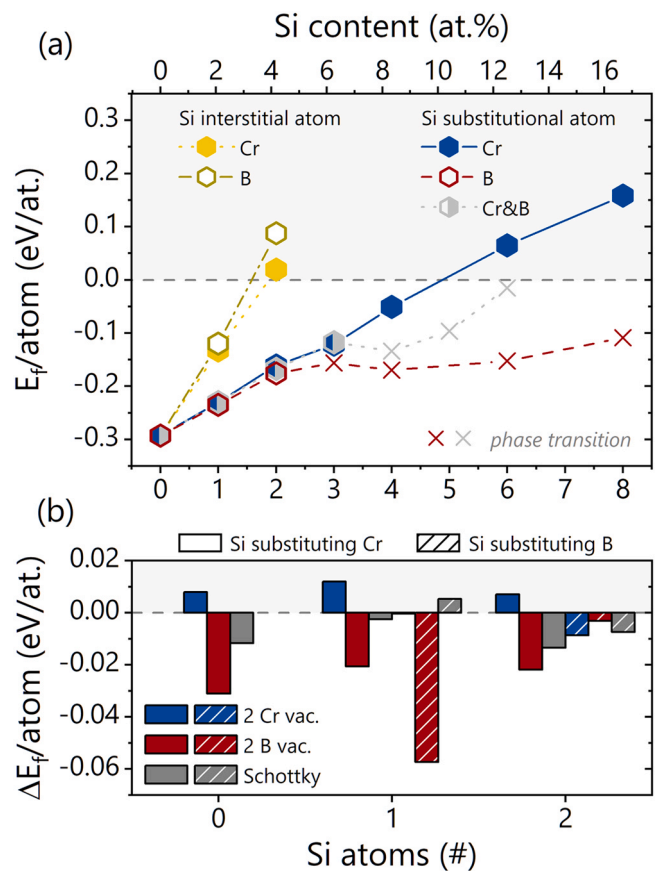

Fig. 1. (a) DFT-calculated E_f per atom for prototypical Cr-Si-B_2 structures (AlB_2-type) with various Si contents. The lower x-axis gives the number of Si atoms within the employed supercell, whereas the upper x-axis gives the corresponding atomic concentration. The Si atoms are either positioned interstitially on Cr- or B-planes, or in substitution for Cr, B, or an equal fraction of both Cr and B atoms. Crossed data points indicate alloying-induced deviations from the prototype structure during supercell relaxation. (b) DFT-evaluated formation energy differences per atom between the prototypical Cr-Si-B_2 structures in (a), with up to two Si atoms replacing either Cr (plane bars) or B (striped bars) atoms in defected structures that hold either two Cr vacancies (blue bars)/ two B vacancies (red bars)/ or one Schottky defect (grey bars), respectively.

beyond 3 atoms (equals values ≥6 at.%), structures with Si substituting solely B atoms and later also upon replacing both B and Cr equally become unstable and undergo a phase transformation (i.e., converge into a different structure type) – see red and grey crosses in Fig. 1a. Only calculations where Si replaces Cr exclusively within the supercell yield negative formation energies up to 4 Si atoms (equals ~8 at.%), while maintaining the hexagonal configuration. In fact, compositions with up to 8 Si alloying atoms on the Cr sublattice relax in the AlB_2-type structure, although thermodynamically unstable due to positive E_f. Consequently, these predictions also indicate a theoretical Si solubility limit within AlB_2-structured CrB_2 above 4 Si atoms, which equals an overall alloying content of about 8 at.%.

Another factor to consider is the presence of point defects, as they are typically related to PVD synthesized films, which can strongly influence the phase stability criteria compared to the thermodynamic equilibrium [41]. Therefore, three different vacancy configurations – either two Cr vacancies, two B vacancies, or one Schottky defect – were analyzed for Cr-Si-B_2 structures with up to 2 alloyed Si atoms. The differences in energy of formation between the defected and the corresponding prototypical structure ($\Delta E_f = E_f^{def} - E_f^{prot}$) are presented in Fig. 1b. In perfect agreement with the findings of Moraes et al. [42], the binary CrB_2 compound favors the formation of boron and boron-containing vacancies over
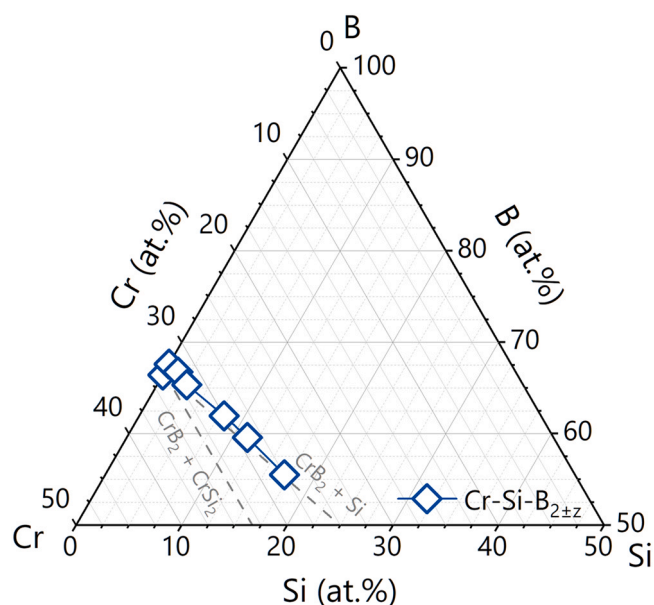
Fig. 2. Ternary phase diagram showing the chemical composition of all synthesized Cr-Si-$B_{2\pm z}$ coatings. The dashed lines connecting CrB_2 with Si and $CrSi_2$ indicate narrow two-phase fields according to the equilibrium phase diagram [43]. The axis ranges are reduced for improved separation of the data points.

Fig. 3. X-ray diffractograms of all Cr-Si-$B_{2\pm z}$ coatings, arranged with increasing Si content from bottom to top. The diffractograms are correlated with standardized reference patterns for hexagonal CrB_2 (space group 191, AlB_2 prototype, [44]) and cubic silicon (substrate material, [45]). The corresponding coating chemistry for each diffractograph is included on the left side.

Cr point defects. The calculations further confirm this trend for both Si alloyed compositions, again indicating the preferred incorporation of B over Cr vacancies, except for the case of two B atoms exchanging Si. There, both vacancy types contribute to increased stability by slightly lowering E_f. Overall, the DFT calculations suggest the preferred incorporation of synthesis induces point defects on the non-metal sublattice for all compositions, with only minor negative influence from transition-metal vacancies.

3.2. Structural & morphological properties

The chemical composition of all Cr-Si-$B_{2\pm z}$ thin films is presented within a ternary phase diagram in Fig. 2. The diagram is extended with guidelines connecting stoichiometric CrB_2 with single-phased Si and $CrSi_2$ (endpoints not visible due to reduced axis ranges), corresponding to narrow two-phase fields according to the equilibrium phase diagram [43]. The chemical analysis revealed an increasing silicon content of 0, 1, 3, 8, 11, and 17 at.% for the alloyed thin films with an increasing number of Si platelets placed on the target racetrack, respectively. The synthesis approach allowed for a predictable and linear adjustment of the Si content within the resulting thin film compositions. The coating prepared with two Si platelets on the target surface obtains an effective Si content below the detection limit of the employed ICP-OES method, thus the coating is referenced with a content of 0 at.% Si ($Cr_{0.32}Si_{0.00}B_{0.68}$). Nevertheless, compared to the unalloyed coating, a minute fraction of Si is still expected within this thin film.

During the PVD deposition of (ternary) compound materials, coatings usually become enriched or depleted in specific constituents due to their preferred sputtering or scattering behavior within the plasma [26]. Interestingly for the Cr-Si-$B_{2\pm z}$ coatings, increasing the Si content in the thin films leads to a stoichiometric (B:Cr = 2:1) replacement of the CrB_2 mole fraction. This is also indicated by the direct overlap of all data points with the connecting line between stoichiometric CrB_2 and pure Si in Fig. 2. Moreover, the Si-free coating $Cr_{0.34}B_{0.66}$ obtains an almost nominal stoichiometry with a B:Cr-ratio close to 2:1, which is consequently preserved for all further Si-containing depositions. Nevertheless, with increasing Si content in the Cr-Si-$B_{2\pm z}$ thin films, the overall B content decreases
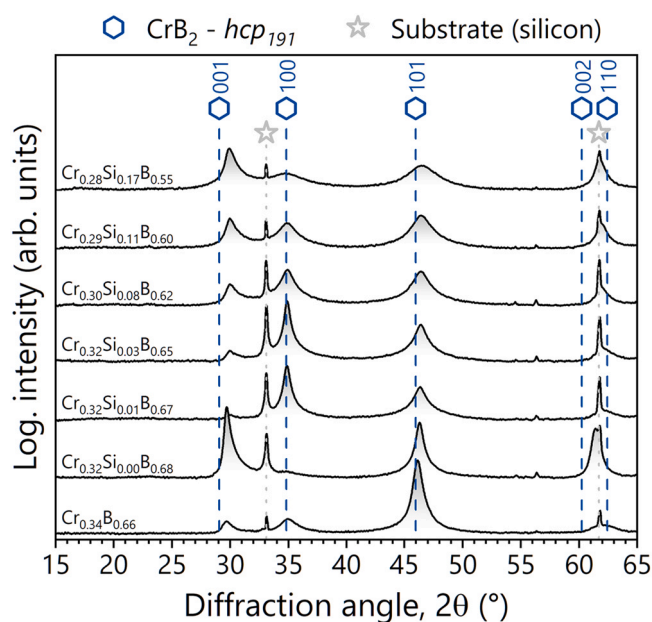
from 66 at.% down to 55 at.% for the coating with the highest Si-content.

The X-ray diffractograms depicted in Fig. 3 demonstrate that all Cr-Si-$B_{2\pm z}$ thin films, regardless of their chemical composition, adopt the hexagonal AlB_2-type structure (space group 191). Moreover, within the accuracy of the employed method, no additional phases could be determined for any coating. All thin films obtain a polycrystalline growth, with slightly preferred orientations noticeable for coatings with a Si content below 8 at.%. Within these samples, the preferred orientation shifts from (101) for the Si-free $Cr_{0.34}B_{0.66}$ coating, towards (001) for $Cr_{0.32}Si_{0.00}B_{0.68}$, to (100)-oriented for both the $Cr_{0.32}Si_{0.01}B_{0.67}$ and $Cr_{0.32}Si_{0.03}B_{0.65}$ thin films, respectively. Further increasing the Si content results in equally oriented grains and causes a reduction of the diffracted intensities, hinting towards a concomitant decrease in the coherently diffracting domains (i.e., a reducing grain size). This structural evolution correlates well with the DFT calculated Si solubility threshold close to 8 at.% (see Fig. 1), thus suggesting that the excess alloying fraction preferably occupies grain boundary sites while also rationalizing their suggested increase in volume fraction due to smaller grains. The data further reveals that incorporating Si into the CrB_2 host structure leads to a slight decrease of the lattice parameter c in (001)-direction from 3.00 to 2.97 Å, meaning that the bond distance between adjacent B and Cr lattice planes is reduced. On the other hand, the lattice parameter a remains relatively unchanged at 2.97 Å, hence lateral bond distances between similar atoms are maintained.

Further correlating the phase formation with the chemical composition of all coatings shows that the decrease in B content with increasing Si fraction takes no influence on the stability of the hexagonal CrB_2 structure in the as deposited state. Considering that only minor quantities of Si are chemically stable when located on the B-sublattice, the missing B-fraction is likely accommodated by introducing vacancies on the non-metal sublattice during the deposition process (compare with Cr-rich/B-deficient planar defects previously observed in $CrB_{1.90}$ [46]). This is also in excellent agreement with the above DFT calculations, where enhanced thermodynamic stability is indicated for all structures containing B-
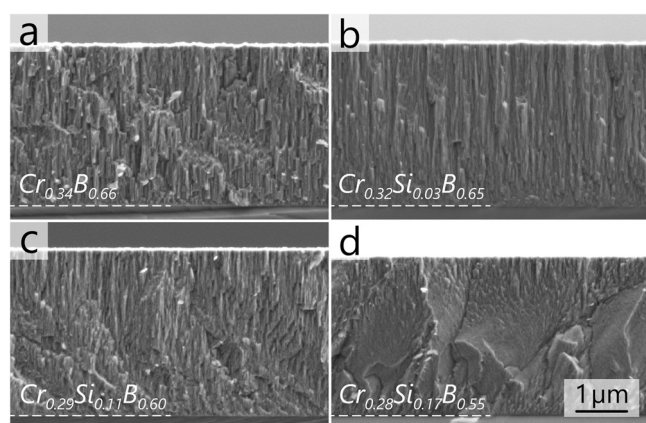
Fig. 4. SEM images depicting the growth morphology of selected Cr-Si-B$_{2\pm z}$ coatings deposited on Si substrate including the corresponding chemical composition.

vacancies – especially pronounced when Si is introduced on the Cr-sublattice.

The influence of Si on the growth mode of Cr-Si-B$_{2\pm z}$ thin films, specifically the decreasing columnar crystallite size, is further illustrated in Fig. 4 through selected SEM fracture cross-sectional studies. The non- and low-alloyed Cr$_{0.34}$B$_{0.66}$ and Cr$_{0.32}$Si$_{0.03}$B$_{0.65}$ coatings show a pronounced columnar structure with grains extending throughout the entire cross-section. The coating with ~11 at.% Si shows denser and increasingly more fibrous crystal columns – see Fig. 4c. With the highest alloying content of 17 at.%, the growth morphology appears featureless, with limited indications for individual columnar structures remaining.

3.3. Atom probe tomography

To obtain an improved view of the distribution of Si atoms within the Cr-Si-B$_{2\pm z}$ thin films – especially at concentrations close to the proposed solubility limit – an additional coating with a composition of Cr$_{0.27}$Si$_{0.09}$B$_{0.64}$ was analogously prepared and investigated using detailed atom probe tomography. Fig. 5 shows reconstructions of the atomic positions for Cr, Si, and B recorded within the tip volume. A random distribution is observed for both Cr and B atoms in the entire volume, although slight clustering of Cr atoms is noticeable in certain regions. In contrast, local chemical analysis of the Si distribution reveals the formation of Si-enriched regions at defect sites, identified as grain boundaries and triple junctions within the as-deposited thin film. A concentration profile in the grain interior (see Fig. 5i and Supplementary) shows an entirely homogeneous distribution of the constitutional elements within the undisturbed, crystalline region. The calculated average chemistry reveals a composition close to Cr$_{0.37}$Si$_{0.04}$B$_{0.60}$, thus indicating that the actual Si solubility within the CrB$_2$-structure could be even lower than the DFT calculated limitation. The corresponding concentration profile taken at a grain boundary location (see Fig. 5ii and Supplementary) depicts an increased fluctuation of all elements and a drastically increased Si content of up to 30 at.% in specific locations. The latter findings clearly underline the preferred segregation of surplus Si during the deposition process.

Overall, these findings experimentally underpin the DFT calculated solubility threshold above 8 at.% Si for the analyzed sample composition. Evidently, the conducted calculations neglect the possible impact of temperature and can only incorporate the chemical as well as kinetic limitations during PVD synthesis to a limited extent, thus rationalizing the deviation from the experimentally observed solubility threshold of ~4 at.%. Nevertheless, within the accuracy of the conducted analysis, the agreement between the chemical composition and DFT calculations is clearly given.

Moreover, the proposed influence of Si segregation to promote grain refinement, as evidenced in XRD analysis above an alloying content of 3 at.%, is additionally confirmed.

3.4. Mechanical properties

Fig. 6 presents the mechanical properties of all Cr-Si-B$_{2\pm z}$ thin films deposited. The residual stress state, film hardness, and Young's modulus are plotted as function of the Si alloying content. The Si-free Cr$_{0.34}$B$_{0.66}$ coating obtains a compressive residual stress state with σ ~ − 0.5 GPa and corresponding hardness and Young's modulus values of H = 23.5 ± 2.7 GPa and E = 295 ± 18 GPa, respectively. When compared to other TMB$_2$ materials, such as TiB$_2$ [47,48] or WB$_2$ [49], CrB$_2$ typically features a reduced hardness and a relatively low elastic modulus [50]. Nevertheless, related works have also reported vastly higher hardness values for this material systems using similar deposition techniques, yet the origin of the observed variation remains unresolved [51–53]. Alloying a minute fraction of Si into CrB$_2$ shows a reversed residual stress state, with Cr$_{0.32}$Si$_{0.00}$B$_{0.68}$ revealing a tensile stress of σ ~ 0.9 GPa. Interestingly, despite the adverse effect of tensile stresses on the measurable hardness, this coating shows identical nanoindentation results with H = 23.9 ± 1.1 and E = 291 ± 6 GPa. The maintained properties are related to the preferred orientation rather than the influence of Si alloying per se. In line with a work by Fuger et al. [54], the preserved hardness is explained by the pronounced orientation towards the (001)-direction (see Fig. 3), which was demonstrated to yield the highest hardness for TMB$_2$ thin films in general. Thus, the anisotropy effect balances the negative impact of the tensile stress state. Consequently, even higher hardness values could be expected for this material system by tailoring the residual stress state towards the compressive regime. The actual shift in the residual stress state between the Cr$_{0.34}$B$_{0.66}$ and Cr$_{0.32}$Si$_{0.00}$B$_{0.68}$ coating may also be related to the preferred orientation. CrB$_2$ obtains a significant anisotropy in the thermal expansion ($\alpha_a^{CrB_2}$ = 10.8 × 10^{-6} K^{-1}, $\alpha_c^{CrB_2}$ = 6.3 × 10^{-6} K^{-1}, [55]), therefore higher in-plane tensile stresses are to be expected for (001)-textured thin film (a-direction parallel to coating-substrate interface) when grown on sapphire substrate ($\alpha_a^{Al_2O_3}$ = 4.5–5.3 × 10^{-6} K^{-1}, [56]). With a further increase in Si, the residual tensile stress is gradually reduced from σ ~ 0.9 GPa for Cr$_{0.32}$Si$_{0.01}$B$_{0.67}$ down to σ ~ 0.3 GPa for Cr$_{0.29}$Si$_{0.11}$B$_{0.60}$, before again increasing in the compressive regime to σ ~ − 0.5 for Cr$_{0.28}$Si$_{0.17}$B$_{0.55}$. Concomitantly, with the above observed increase in grain boundary volume – i.e., an increase in regions that are less strongly bound than the surrounding crystal – a linear decrease in the elastic modulus down to E = 238 ± 7 GPa for the highest Si content of 17 at.% was recorded. Interestingly, Si alloying did not result in any solid solution hardening effect during nanoindentation. Upon introducing more than 1 at.% Si into CrB$_2$, the hardness gradually decreases from H = 21.6 ± 1.1 GPa for Cr$_{0.32}$Si$_{0.01}$B$_{0.67}$, down to a constant value of H ~ 17 GPa for all coatings having a Si content ≥ 8 at.%. In relation to the Si segregations observed on grain boundaries for higher alloying compositions (see Fig. 5), the measured hardness of these thin films is likely dominated by the inferior mechanical properties of the Si-rich regions.

3.5. Dynamic oxidation

Dynamic oxidation experiments were conducted in a TGA system to revisit [28] the impact of Si alloying on the high-temperature oxidation resistance of CrB$_2$-based thin films, and to determine the minimum alloying quantity necessary to yield enhanced protective properties. Fig. 7 presents the mass change of the coating material, deposited onto pre-weighed polycrystalline Al$_2$O$_3$ substrate (inert in the temperature rage up to 1400 °C, [28]), with respect to the annealing temperature T. Up to a range of T ~ 600 °C a constant mass
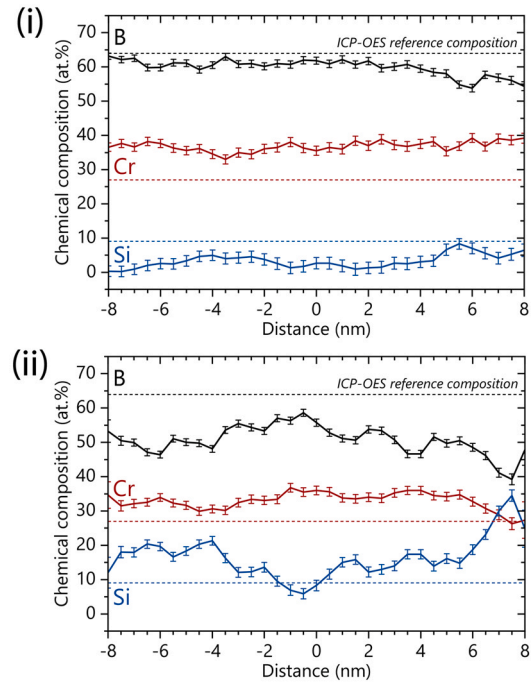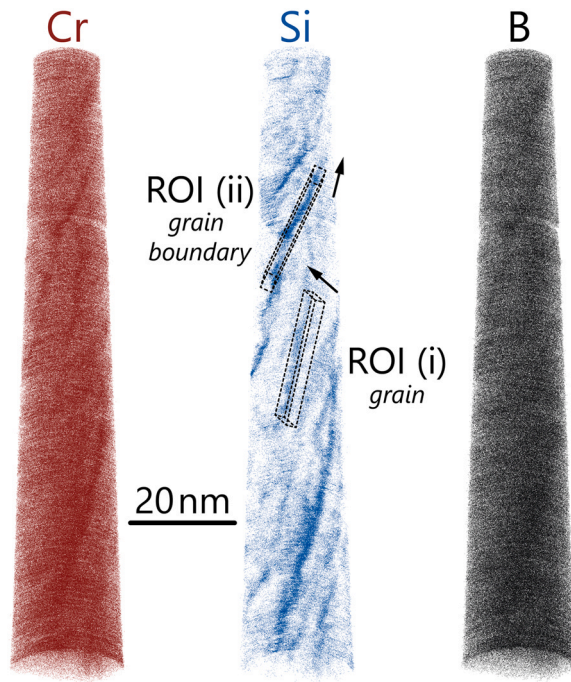
Fig. 5. Atom probe tomography determined chemical composition of a $Cr_{0.27}Si_{0.09}B_{0.64}$ thin film. Reconstructed positions of Cr, Si, and B atoms are presented. Insets (i) and (ii) depict concentration profiles of the grain interior and grain boundary, respectively. Both profiles were collected in the corresponding regions of interest marked in the Si atom distribution. The supplementary material contains animations of the Si distribution to provide an improved view on both regions of interest.
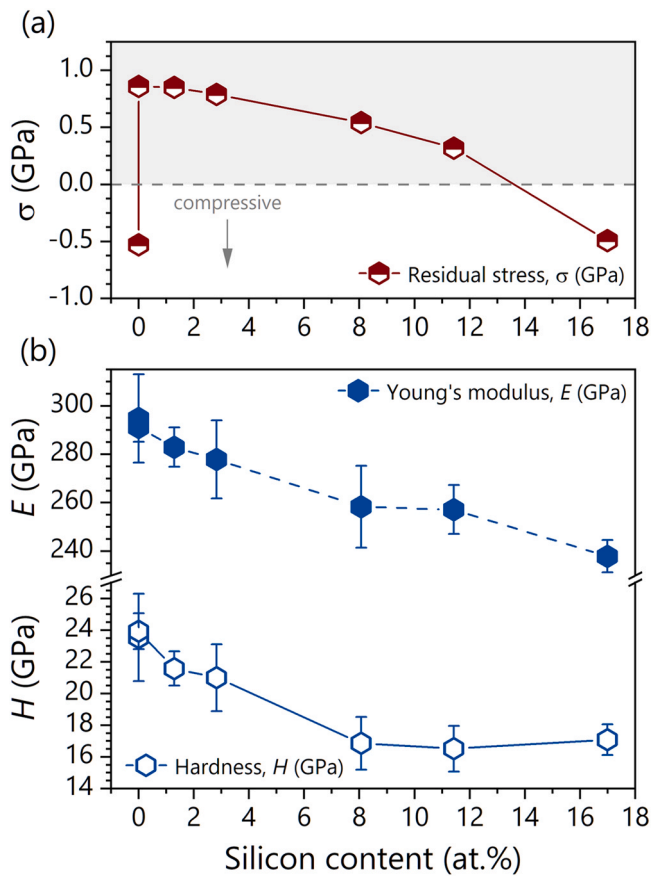

Fig. 6. (a) Residual stress state of all Cr-Si-$B_{2\pm z}$ thin films versus the Si alloying content. (b) Corresponding hardness and Young's modulus data. All mechanical properties were determined on coated sapphire substrates.
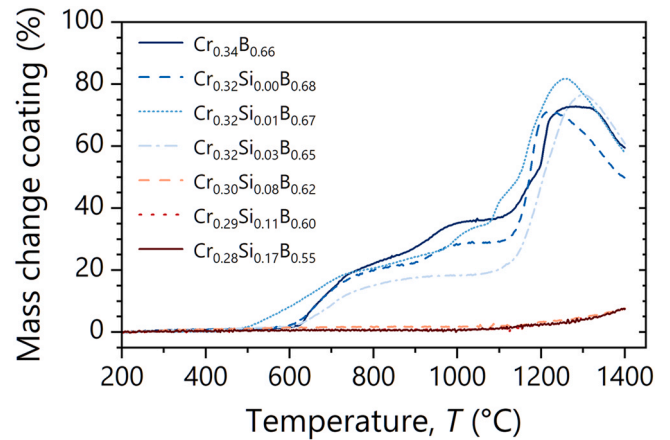

Fig. 7. Mass change of all Cr-Si-$B_{2\pm z}$ coatings as function of the annealing temperature, recorded during dynamic oxidation in a TGA system (10 K/min heating rate) in synthetic air environment. The coatings were deposited on pre-weighed Al_2O_3 substrates, which are inert over the entire temperature range.

signal is recorded for all Cr-Si-$B_{2\pm z}$ thin films, indicating no progressive oxide scale formation. Only the $Cr_{0.32}Si_{0.01}B_{0.67}$ thin film shows an earlier onset temperature at $T \sim 500\,°C$ (blue dotted line), visible by the already occurring mass gain due to oxide scale growth. Upon reaching the oxidation onset temperature, all Cr-Si-$B_{2\pm z}$ coatings up to a Si content of 3 at.% show a stepwise increase in the mass signal until reaching a maximum value at $T \sim 1200\,°C$, indicating the fully oxidized state. Beyond this temperature, a decreasing sample mass is recorded, which is correlated with the evaporation of B_2O_3-based oxides. The mass signal evolution shows intermediate plateaus for all these coatings between $600 < T < 1200\,°C$, hinting towards a competitive formation of B_2O_3- and Cr_2O_3-based scales and thus limited protection against continued oxidation. Moreover, with already small alloying fractions (e.g., $Cr_{0.32}Si_{0.03}B_{0.65}$), both the slope of the increase and the overall

mass gain up to $T \sim 1100\,°C$ are significantly reduced, already pointing towards the effectiveness of the employed alloying routine.

Increasing the Si content within the Cr-Si-$B_{2\pm z}$ thin films beyond 8 at.% leads to a fully preserved coating mass up to $T \sim 1100\,°C$ due to the formation of a stable, protective oxide scale preventing any oxidative attack of the underlying coating material. Only at $T > 1100\,°C$, these higher alloyed thin films show a slight increase in the overall mass signal up to $1400\,°C$. Unlike the low-alloyed coatings, the protective mechanism relies on the formation of a continuous, dense SiO_2-based scale enabled by a sufficient Si diffusion provided through the Cr-Si-$B_{2\pm z}$ thin film. Moreover, as known for a $Cr_{0.26}Si_{0.16}B_{0.58}$ coating [28], the formed oxide scale after annealing at $T = 1400\,°C$ should in fact be comprised of a layered amorphous SiO_2-based phase with a crystalline Cr_2O_3 scale on top (discussed in more detail in Section 3.7). Overall, these results highlight that achieving high-temperature oxidation resistance for Cr-Si-$B_{2\pm z}$ thin films involves a minimum alloying content close to 8 at.% Si to activate the protective mechanism.

3.6. In-situ X-ray diffraction

Comparative in-situ X-ray diffraction studies were performed during the oxidation of $Cr_{0.32}Si_{0.03}B_{0.65}$ and $Cr_{0.29}Si_{0.11}B_{0.60}$ in lab-air environment, to reveal the underlying mechanism causing the drastically improved oxidation resistance above a distinct Si content. Fig. 8 depicts the diffractographs taken at room temperature (RT) as well as from 400 to 1200 °C in steps of 50 °C, with the corresponding annealing temperature included on the right axis. The data for an "insufficiently" alloyed $Cr_{0.32}Si_{0.03}B_{0.65}$ coating (see Fig. 8a) reveal an unaltered crystal structure up to a temperature of $T = 550\,°C$, depicting a preferred (100)-orientation as shown in Fig. 3. With the oxidation onset at $T = 600\,°C$ (see also Fig. 7), initial indications towards a boron depleted CrB phase are formed (e.g., $2\theta \sim 32.2°$, $38.5°$, $44.9°$, etc.), increasing in intensity up to $T = 1100\,°C$. This suggests the partial decomposition of the Cr-Si-B_2 structure to form an unprotective B_2O_3 scale, which is in line with the mass gain to an initial plateau observed during the TGA measurements. In the temperature regime beyond $T = 750–800\,°C$, additional recrystallization of the remaining Cr-Si-$B_{2\pm z}$ solid solution is observed, as indicated by the decreasing peak width and increase in diffracted intensities (e.g., $2\theta \sim 45.8°$). Similar behavior was previously reported for amorphous Cr-Al-Si-B-(N) coatings, experiencing crystallization of the CrB_2 phase at $T = 800\,°C$ [57]. At $T = 1050\,°C$ the diffraction signals for the CrB_2 structure diminish, pointing towards a full decomposition of the diboride phase. Finally, at $T = 900\,°C$, an additional Cr_2O_3 scale is formed – compare with the second mass gain plateau observed in Fig. 7 – which subsequently consumes the entire coating at $T = 1200\,°C$. Over the entire temperature range, no Si-based phase is observed.

A direct comparison to results obtained for a "sufficiently" alloyed $Cr_{0.29}Si_{0.11}B_{0.60}$ (Si content $\geq \sim 8$ at.%) coating is illustrated in Fig. 8b. In the as-deposited state at RT, the data shows an analogous diffraction result as depicted in Fig. 3, revealing a hexagonal structured CrB_2-based coating with polycrystalline grain distribution. Moreover, no additional Cr-Si- or Si-B-based phase is detected, suggesting that Si is dissolved up to the solubility limit of $\sim 3–4$ at.%

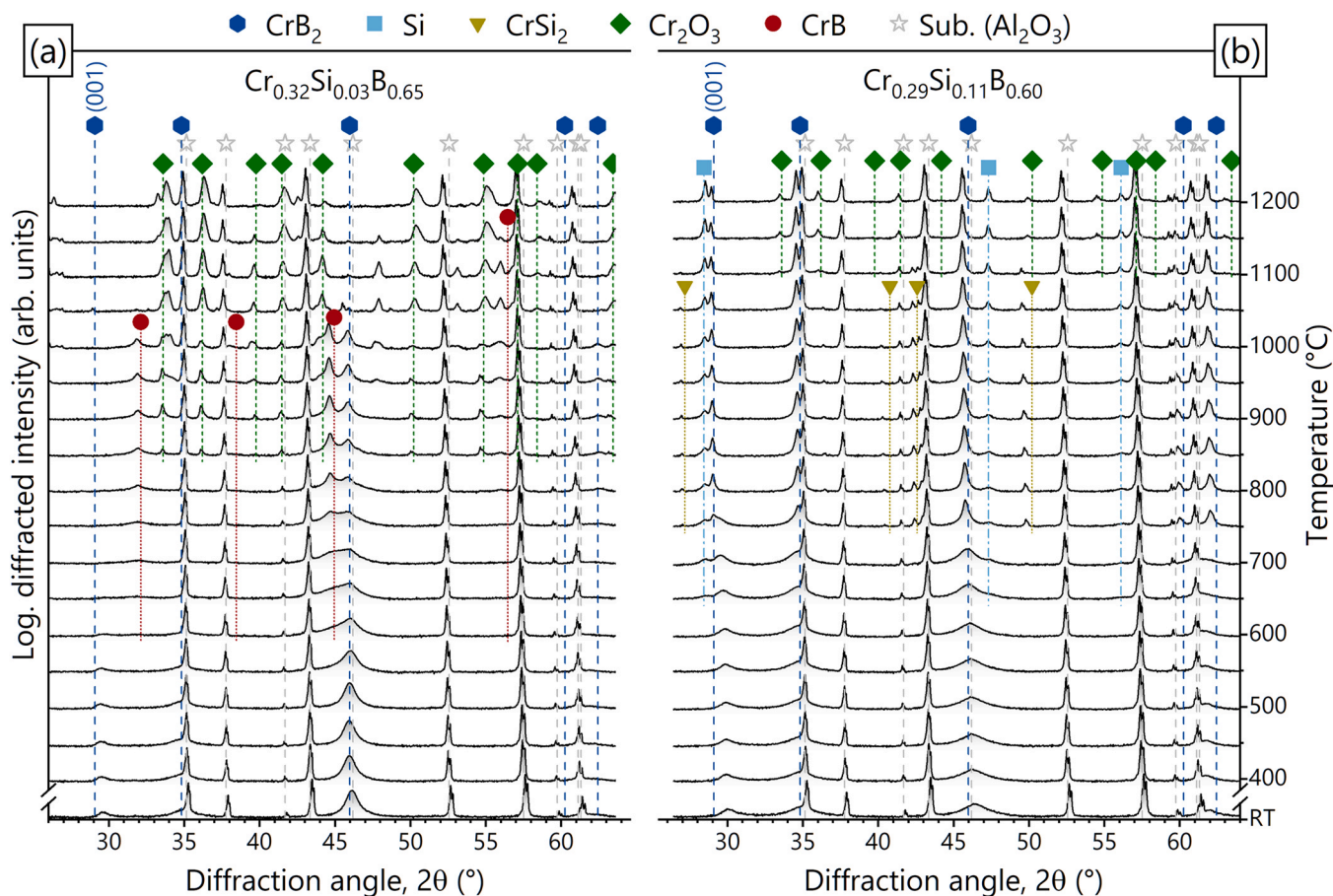**Fig. 8.** In-situ X-ray diffractographs recorded during subsequent annealing treatments in lab-air environment of (a) $Cr_{0.32}Si_{0.03}B_{0.65}$ and (b) $Cr_{0.29}Si_{0.11}B_{0.60}$ thin films deposited on polycrystalline Al_2O_3. Standardized reference patterns for hexagonal CrB_2 (blue hexagon, [44]), cubic Si (light blue square, [45]), hexagonal $CrSi_2$ (dark yellow triangle, [58]), rhombohedral Cr_2O_3 (green diamond, [59]), orthorhombic CrB (dark red circle, [60]) and rhombohedral Al_2O_3 (grey star, [61]) are included. The sample temperature corresponding to each diffraction experiment is added on the right axis.
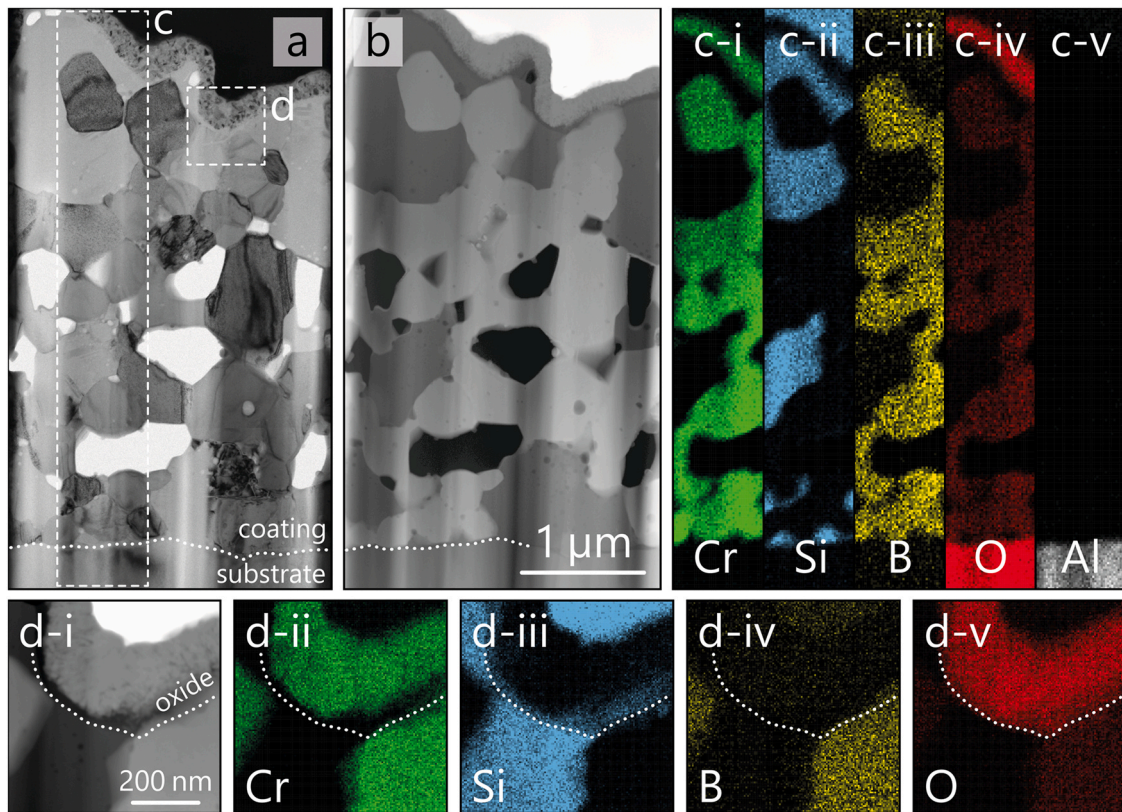
Fig. 9. (a) bright-field and (b) high-angle annular dark field TEM micrographs of a $Cr_{0.29}Si_{0.11}B_{0.60}$ coating on polycrystalline Al_2O_3 substrate, gradually oxidized up to 1200 °C (see Fig. 8). (c) elemental EDX mapping of the entire sample cross-section according to the insert in (a). (d) detailed scanning-TEM image of the oxide scale indicated in (a) including the elemental EDX mapping.

within the CrB_2 structure – note that excess Si is located at grain boundaries as shown in Fig. 5. The structure is fully preserved up to a temperature of $T = 600$ °C. A further increase to $T = 650$ °C leads to first indications for crystalline Si precipitates (e.g., $2\theta \sim 28.7°$, $47.5°$, $56.3°$). Analogously to $Cr_{0.32}Si_{0.03}B_{0.65}$, recrystallization of the CrB_2 structure is observed beyond $T = 750$–800 °C (e.g., $2\theta \sim 29.0°$, $34.7°$, $45.8°$, etc.), being more pronounced due to the absence of a CrB phase. Furthermore, in accordance with the three-phase field of CrB_2-$CrSi_2$-Si in Fig. 2 (area between the dashed lines), the intermediate formation of a $CrSi_2$ phase is suggested between $T = 750$ and 1050 °C by a set of low intensity reflexes (e.g., $2\theta \sim 26.8°$, $42.3°$, $49.6°$). However, it should be noted that the deviation from the indexed peak positions is significant, so that additional high-resolution analysis would be required for confirmation. Recrystallization of the Cr-Si-$B_{2 \pm z}$ matrix and Si precipitation continue up to $T = 1200$ °C, resulting in sharp peaks for both phases. In addition, several indications for a Cr_2O_3 oxide layer emerge after the annealing experiments above $T \geq 1100$ °C (e.g., $2\theta \sim 33.5°$, $50.0°$, $54.5°$), yet no diffraction peaks pointing towards a B_2O_3 or the more important SiO_2-based structure occur. Thus, in line with previous findings, especially the latter phase is expected to be in an amorphous state. Overall, pronounced diffraction peaks indicate that the original Cr-Si-$B_{2 \pm z}$ structure is still intact at $T = 1200$ °C, highlighting the excellent oxidation resistance of this coating and confirming the presence of a stable oxide scale protecting the underlying coating material.

When discussed in relation to the dynamic oxidation experiments (see Fig. 7), the precipitation of Si at $T > 600$ °C in this "sufficiently" alloyed coating correlates well with the oxidation onset temperature of the "insufficiently" alloyed samples. Consequently, this provides a strong indication that Si precipitates within the $Cr_{0.29}Si_{0.11}B_{0.60}$ coating – either derived from excess Si on grain boundaries or the surrounding Cr-Si-$B_{2 \pm z}$ solid solution (discussed in more detail in Section 3.7) – are the primary source for the increased oxidation resistance. In addition, the formation of crystalline Cr_2O_3 above $T = 1100$ °C is in excellent agreement with the previous TGA analysis, rationalizing the mass gain for all coatings with Si content above 8 at.% in the same temperature regime.

Regarding the thermally activated precipitation of Si from the $Cr_{0.29}Si_{0.11}B_{0.60}$ coating, a possible explanation is seen in the continuous increase in the DFT calculated E_f for the AlB_2 structured Cr-Si-B_2 compositions over the binary CrB_2 with increasing Si content. Theoretically comparing the difference in energy of formation between a $Cr_{0.27}Si_{0.06}B_{0.67}$ structure (see Fig. 1) with its corresponding decomposition products of CrB_{2+z} and Si according to:

$$\Delta E_f = [(1 - x) E_f^{CrB_2} + x E_f^{Si} + 2x E_f^{B}] - E_f^{Cr_{0.27}Si_{0.06}B_{0.67}},$$

with $x = 0.06$ \hfill (1)

a significant energetic benefit of $\Delta E_f = -1.34$ eV/at. towards the decomposed constituents is attained. The DFT calculated formation energies of elemental Si (cubic, -5.41 eV/at.) and B (rhombohedral, -6.67 eV/at.) correspond to their stable configuration at room-temperature and ambient pressure.

Analogous results are obtained for all other theoretically and experimentally studied compositions of Cr-Si-$B_{2 \pm z}$, thus underlining that the precipitation follows the thermodynamically prescribed equilibrium condition. Finally, the precipitation is believed to be further supported during recrystallization of the Cr-Si-$B_{2 \pm z}$ phase above $T = 750$–800 °C, allowing for even enhanced Si diffusion. Considering a melting temperature of $T_M = 2200$ °C [62] for pure CrB_2, the recrystallization process occurs at a typical homologous temperature of $T_H \sim 0.4$.

3.7. Structural & chemical analysis post annealing

In order to complete the established viewpoint on the morphological evolution and especially the oxide scale growth during high-temperature oxidation of Cr-Si-B$_{2\pm z}$ thin films, complementary detailed TEM analysis (see Fig. 9) is performed on the Cr$_{0.29}$Si$_{0.11}$B$_{0.60}$ thin film used during the in-situ X-ray studies (see Fig. 8b). Fig. 9a and b depict bright-field and high-angle annular dark field micrographs of the entire sample cross-section, including the interface to the polycrystalline Al$_2$O$_3$ substrate and the formed oxide scale, respectively. Both images immediately visualize the pronounced recrystallization of the Cr-Si-B$_{2\pm z}$ thin film, revealing large globular grains throughout the cross-section. Given the atomic number contrast in the HAADF image, regions of different elemental compositions – indicated by lighter and darker grey areas – can be identified next to several black appearing voids. When combined with the elemental mapping in Fig. 9c, bright areas can be correlated with a Cr- and B-rich phase (i.e., CrB$_{2\pm z}$), whereas darker regions correspond exclusively to pure Si. Note the superposition of Cr and O signals during EDX analysis, thus creating a slight, artificial O signal (see Fig. 9c-iv) overlapping with all CrB$_{2\pm z}$ regions. Furthermore, also Si and W overlap in the EDX spectrum, resulting in a misinterpretation of the W protection layer with an artificial Si region in the top area of Fig. 9c-ii. Several conclusions can be drawn from these results: (*i*) Silicon precipitation is not restricted to grain boundary sites already holding excess Si in the as-deposited state. (*ii*) Upon thermal activation, the Cr-Si-B$_{2\pm z}$ solid solution fully decomposes into large globular phase regions containing solely CrB$_{2\pm z}$ or Si. (*iii*) Globular Si precipitates are formed throughout the coating cross-section in addition to a continuous surface layer. As a result, several voids are formed in the thin film volume to compensate for the Si surface diffusion (note, certain voids may also originate from focus-ion beam milling preparation of the TEM lamella, resulting from the weak connection between the individual recrystallized grains). Finally, the elemental distributions of Al and O show that no interaction between the coating and substrate material occurred during the entire oxidation treatment.

Fig. 9a and b also clearly show a thin, dense oxide scale formed on the sample surface. Using detailed STEM imaging combined with EDX analysis (see Fig. 9d), the oxide reveals a defined, layered architecture composed of a thin amorphous SiO$_2$ layer on the coating-oxide interface and a nanocrystalline Cr$_2$O$_3$ top layer. Similar to the elemental distribution in Fig. 9c, no intermixing of Cr- and B-rich sites with Si can be observed in the oxide layer and the unaffected material below. However, it has to be considered that the employed chemical analysis is not suitable for tracing minimum quantities of light elements such as B within, e.g., the SiO$_2$ layer. Interestingly, despite the extended annealing time at temperatures above $T > 1000$ °C, the SiO$_2$ layer features a thickness in the range of only 20–40 nm, whereas the Cr$_2$O$_3$ top layer extends over 200–250 nm.

Regarding the temporal sequence of forming the highly protective oxide scale, the primary mechanism is seen in the precipitation of Si – especially towards the coating surface – allowing for the initial growth of a stable SiO$_2$ layer in the temperature range from $T = 650$–1100 °C. Due to the minimal thickness of this layer, even at $T = 1200$ °C, no mass gain is visible in the TGA signal. Furthermore, in line with the TGA and in-situ X-ray diffraction analysis, the additional Cr$_2$O$_3$ surface layer is subsequently formed in the temperature regime above $T = 1100$ °C. Unlike many TM-oxides, Cr-cations primarily diffuse outwards on grain boundaries within the Cr$_2$O$_3$ oxide layer, thus allowing for a scale growth on top of the oxide surface rather than the oxide-coating interface [63]. Also, resulting from the vastly increased layer thickness, the formation is clearly relatable to the mass gain signal shown in Fig. 7.

4. Conclusion

Si alloying was proven a successful concept to significantly enhance the oxidation resistance of transition-metal diboride-based thin films. In this work, DC magnetron sputtered Cr-Si-B$_{2\pm z}$ coatings with Si content up to 17 at.% were analyzed to reveal the impact of the alloying element on the structural and mechanical properties of the AlB$_2$-type thin films. In addition, the mechanisms leading to the enhanced oxidation resistance were investigated to deepen the knowledge on optimized chemical compositions.

DFT calculations performed on various stoichiometric and defected AlB$_2$-structured Cr-Si-B$_2$ compositions indicate the energetically favored incorporation of Si on the Cr-sublattice over a wide alloying range. Contrary, already limited occupation of the B-sublattice destabilizes the hexagonal cell. Detailed APT analysis of a Cr$_{0.27}$Si$_{0.09}$B$_{0.64}$ thin film revealed Si segregation towards grain boundaries in the as-deposited state, while the grain interior holds up to 4 at.% Si, being in line with a DFT-calculated solubility limit.

Despite a concomitant increase in B under-stoichiometry with increasing Si content, all synthesized Cr-Si-B$_{2\pm z}$ coatings obtain the hexagonal AlB$_2$ structure, irrespective of the chemical composition. Moreover, increasing the Si content is accompanied by a variation of the preferred growth orientation and a gradual reduction in the average columnar grain size. Nanoindentation measurements showed a direct correlation between the morphological features and the mechanical properties. The highest film hardness was recorded for low Si alloyed, (001)-oriented coatings at $H \sim 24$ GPa, whereas an increased alloying content of Si ≥ 8 at.% resulted in $H \sim 17$ GPa due to mechanically weak Si grain boundary segregates.

Thermogravimetric analysis proofed the excellent oxidation resistance of Cr-Si-B$_{2\pm z}$ thin films with Si content ≥ 8 at.% up to $T \sim 1400$ °C, whereas lower alloyed coatings suffer from stepwise oxidation above $T \sim 600$ °C related to a non-protecting Cr- and B-based oxide scale. The enhanced oxidation resistance could be linked to thermally activated precipitation of Si and the subsequent recrystallization of the Cr-Si-B$_{2\pm z}$ solid solution, thereby creating a continuous Si-based surface layer. This layer allows for a dense, amorphous SiO$_2$-based scale (~ 20 nm at 1200 °C) in the temperature range between $T = 650$–1100 °C, beyond which an additional nanocrystalline Cr$_2$O$_3$ top layer (~ 200 nm at 1200 °C) is formed due to increased Cr-outward diffusion.

In summary, the results underpin the promising capabilities of Cr-Si-B$_{2\pm z}$ coatings applied in high-temperature oxidative environments and provide detailed guidelines to connect the chemical composition with resulting thin film properties.

CRediT authorship contribution statement

L. Zauner: Conceptualization, Investigation, Visualization, Writing – original draft. **A. Steiner:** Investigation, Writing – review & editing. **T. Glechner:** Investigation, Writing – review & editing. **A. Bahr:** Investigation, Writing – review & editing. **B. Ott:** Investigation, Writing – review & editing. **R. Hahn:** Investigation, Writing – review & editing. **T. Wojcik:** Investigation, Writing – review & editing. **O. Hunold:** Project administration, Writing – review & editing. **J. Ramm:** Conceptualization, Project administration, Writing – review & editing. **S. Kolozsvári:** Project administration, Writing – review & editing. **P. Polcik:** Conceptualization, Project administration, Writing – review & editing. **P. Felfer:** Investigation, Writing – review & editing. **H. Riedl:** Supervision, Conceptualization, Project administration, Writing – review & editing.

Data Availability

Data will be made available on request.

Declaration of Competing Interest

Acknowledgments

Appendix A. Supporting information

Supplementary data associated with this article can be found in the online version at doi:10.1016/j.jallcom.2023.169203.

References

[1] C..Subramanian, A.K..Suri, T.S.R..Ch.Murthy, Development of Boron-based materials for nuclear applications, BARC Newsl. (2010) 6–9. https://inis.iaea.org/search/search.aspx?orig_q=RN:45027141 (Accessed 18 August 2022).

[2] D. Sciti, L. Silvestroni, L. Mercatelli, J.L. Sans, E. Sani, Suitability of ultra-refractory diboride ceramics as absorbers for solar energy applications, Sol. Energy Mater. Sol. Cells 109 (2013) 8–16, https://doi.org/10.1016/j.solmat.2012.10.004

[3] D.C. Larbalestier, L.D. Cooley, M.O. Rikel, A.A. Polyanskii, J. Jiang, S. Patnaik, X.Y. Cai, D.M. Feldmann, A. Gurevich, A.A. Squitieri, M.T. Naus, C.B. Eom, E.E. Hellstrom, R.J. Cava, K.A. Regan, N. Rogado, M.A. Hayward, T. He, J.S. Slusky, P. Khalifah, K. Inumaru, M. Haas, Strongly linked current flow in polycrystalline forms of the superconductor MgB2, Nature 410 (2001) 186–189, https://doi.org/10.1038/35065559

[4] F. Monteverde, L. Scatteia, Resistance to thermal shock and to oxidation of metal diborides-SiC ceramics for aerospace application, J. Am. Ceram. Soc. 90 (2007) 1130–1138, https://doi.org/10.1111/j.1551-2916.2007.01589.x

[5] M. Magnuson, L. Hultman, H. Högberg, Review of transition-metal diboride thin films, Vacuum 196 (2022) 110567, https://doi.org/10.1016/j.vacuum.2021.110567

[6] A. Bellosi, F. Monteverde, Fabrication and properties of zirconium diboride-based ceramics for UHT applications, in: Eur. Sp. Agency, (Special Publ. ESA SP, 2003: pp. 65–72. https://www.researchgate.net/publication/234354208 (Accessed 18 August 2022).

[7] W. Tan, C.A. Petorak, R.W. Trice, Rare-earth modified zirconium diboride high emissivity coatings for hypersonic applications, J. Eur. Ceram. Soc. 34 (2014) 1–11, https://doi.org/10.1016/j.jeurceramsoc.2013.07.016

[8] C. Rhodes, J. Stuart, R. Lopez, X. Li, M. Waje, M. Mullings, J. Lau, S. Licht, Evaluation of properties and performance of nanoscopic materials in vanadium diboride/air batteries, J. Power Sources 239 (2013) 244–252, https://doi.org/10.1016/j.jpowsour.2013.03.071

[9] W.G. Fahrenholtz, G.E. Hilmas, Ultra-high temperature ceramics: materials for extreme environments, Scr. Mater. 129 (2017) 94–99, https://doi.org/10.1016/j.scriptamat.2016.10.018

[10] C. Mitterer, Borides in thin film technology, J. Solid State Chem. 133 (1997) 279–291, https://doi.org/10.1006/jssc.1997.7456

[11] J.W. Zimmermann, G.E. Hilmas, W.G. Fahrenholtz, R.B. Dinwiddie, W.D. Porter, H. Wang, Thermophysical properties of ZrB2 and ZrB2-SiC ceramics, J. Am. Ceram. Soc. 91 (2008) 1405–1411, https://doi.org/10.1111/j.1551-2916.2008.02268.x

[12] V. Moraes, L. Zauner, T. Wojcik, M. Arndt, P. Polcik, H. Riedl, P.H. Mayrhofer, Thermally stable superhard diborides: An ab initio guided case study for V-W-diboride thin films, Acta Mater. 186 (2020) 487–493, https://doi.org/10.1016/j.actamat.2020.01.014

[13] C. Fuger, V. Moraes, R. Hahn, H. Bolvardi, P. Polcik, H. Riedl, P.H. Mayrhofer, Influence of Tantalum on phase stability and mechanical properties of WB 2, MRS Commun. 9 (2019) 375–380, https://doi.org/10.1557/mrc.2019.5

[14] C. Fuger, B. Schwartz, T. Wojcik, V. Moraes, M. Weiss, A. Limbeck, C.A. Macauley, O. Hunold, P. Polcik, D. Primetzhofer, P. Felfer, P.H. Mayrhofer, H. Riedl, Influence of Ta on the oxidation resistance of WB2−z coatings, J. Alloy. Compd. 864 (2021) 158121, https://doi.org/10.1016/j.jallcom.2020.158121

[15] B. Bakhit, J. Palisaitis, J. Thörnberg, J. Rosen, P.O.Å. Persson, L. Hultman, I. Petrov, J.E. Greene, G. Greczynski, Improving the high-temperature oxidation resistance of TiB2 thin films by alloying with Al, Acta Mater. 196 (2020) 677–689, https://doi.org/10.1016/j.actamat.2020.07.025

[16] J. Thörnberg, S. Mráz, J. Palisaitis, F.F. Klimashin, P. Ondracka, B. Bakhit, P. Polcik, S. Kolozsvari, L. Hultman, I. Petrov, P.O.Å. Persson, J.M. Schneider, J. Rosen, Oxidation resistance and mechanical properties of sputter-deposited Ti0.9Al0.1B2-y thin films, Surf. Coat. Technol. 442 (2022) 128187, https://doi.org/10.1016/j.surfcoat.2022.128187

[17] A.H. Navidi Kashani, S. Mráz, D.M. Holzapfel, M. Hans, L. Löfler, P. Ondračka, D. Primetzhofer, J.M. Schneider, Synthesis and oxidation behavior of Ti0.35Al0.65By (y = 1.7–2.4) coatings, Surf. Coat. Technol. 442 (2022) 128190, https://doi.org/10.1016/j.surfcoat.2022.128190

[18] T.A. Parthasarathy, R.A. Rapp, M. Opeka, R.J. Kerans, A model for the oxidation of ZrB2, HfB2 and TiB2, Acta Mater. 55 (2007) 5999–6010, https://doi.org/10.1016/j.actamat.2007.07.027

[19] W.G. Fahrenholtz, G.E. Hilmas, Oxidation of ultra-high temperature transition metal diboride ceramics, Int. Mater. Rev. 57 (2012) 61–72, https://doi.org/10.1179/1743280411Y.0000000012

[20] L. Silvestroni, K. Stricker, D. Sciti, H.J. Kleebe, Understanding the oxidation behavior of a ZrB2–MoSi2 composite at ultra-high temperatures, Acta Mater. 151 (2018) 216–228, https://doi.org/10.1016/j.actamat.2018.03.042

[21] I.G. Talmy, J.A. Zaykoski, M.M. Opeka, High-temperature chemistry and oxidation of ZrB 2 ceramics containing SiC, Si 3N 4, Ta 5Si 3, and TaSi 2, J. Am. Ceram. Soc. 91 (2008) 2250–2257, https://doi.org/10.1111/j.1551-2916.2008.02420.x

[22] T.S.R.C. Murthy, J.K. Sonber, C. Subramanian, R.K. Fotedar, M.R. Gonal, A.K. Suri, Effect of CrB2 addition on densification, properties and oxidation resistance of TiB2, Int. J. Refract. Met. Hard Mater. 27 (2009) 976–984, https://doi.org/10.1016/j.ijrmhm.2009.06.004

[23] B. Bakhit, S. Dorri, A. Kooijman, Z. Wu, J. Lu, J. Rosen, J.M.C. Mol, L. Hultman, I. Petrov, J.E. Greene, G. Greczynski, Multifunctional ZrB2-rich Zr1-xCrxBy thin films with enhanced mechanical, oxidation, and corrosion properties, Vacuum 185 (2021), https://doi.org/10.1016/j.vacuum.2020.109990

[24] S. Dorri, J. Palisaitis, G. Greczynski, I. Petrov, J. Birch, L. Hultman, B. Bakhit, Oxidation kinetics of overstoichiometric TiB2 thin films grown by DC magnetron sputtering, Corros. Sci. 206 (2022) 110493, https://doi.org/10.1016/J.CORSCI.2022.110493

[25] J. Thörnberg, B. Bakhit, J. Palisaitis, N. Hellgren, L. Hultman, G. Greczynski, P.O.Å. Persson, I. Petrov, J. Rosen, Improved oxidation properties from a reduced B content in sputter-deposited TiBx thin films, Surf. Coat. Technol. 420 (2021) 127353, https://doi.org/10.1016/j.surfcoat.2021.127353

[26] C. Fuger, R. Hahn, A. Hirle, P. Kutrowatz, M. Weiss, A. Limbeck, O. Hunold, P. Polcik, H. Riedl, Revisiting the origins of super-hardness in TiB2+z thin films – impact of growth conditions and anisotropy, Surf. Coat. Technol. 446 (2022) 128806, https://doi.org/10.1016/j.surfcoat.2022.128806

[27] T. Glechner, O.E. Hudak, T. Wojcik, L. Haager, F. Bohrn, H. Hutter, O. Hunold, J. Ramm, S. Kolozsvári, E. Pitthan, D. Primetzhofer, H. Riedl, Influence of the non-metal species on the oxidation kinetics of Hf, HfN, HfC, and HfB2 coatings, Mater. Des. 211 (2021) 110136, https://doi.org/10.1016/j.matdes.2021.110136

[28] T. Glechner, H.G. Oemer, T. Wojcik, M. Weiss, A. Limbeck, J. Ramm, P. Polcik, H. Riedl, Influence of Si on the oxidation behavior of TM-Si-B2 ± z coatings (TM = Ti, Cr, Hf, Ta, W), Surf. Coat. Technol. 434 (2022) 128178, https://doi.org/10.1016/j.surfcoat.2022.128178

[29] T. Glechner, A. Bahr, R. Hahn, T. Wojcik, M. Heller, A. Kirnbauer, J. Ramm, S. Kolozsvari, P. Felfer, H. Riedl, High temperature oxidation resistance of physical vapor deposited Hf-Si-B2 ± z thin films, Corros. Sci. 205 (2022) 110413, https://doi.org/10.1016/j.corsci.2022.110413

[30] B. Grančič, M. Mikula, T. Roch, P. Zeman, L. Satrapinskyy, M. Gregor, T. Plecenik, E. Dobročka, Z. Hájovská, A. Mičušík, A. Šatka, M. Zahoran, A. Plecenik, P. Kúš, Effect of Si addition on mechanical properties and high temperature oxidation resistance of Ti-B-Si hard coatings, Surf. Coat. Technol. 240 (2014) 48–54, https://doi.org/10.1016/j.surfcoat.2013.12.011

[31] W.C. Oliver, G.M. Pharr, Measurement of hardness and elastic modulus by instrumented indentation: Advances in understanding and refinements to methodology, J. Mater. Res. 19 (2004) 3–20, https://doi.org/10.1557/jmr.2004.19.1.3

[32] A.C. Fischer-Cripps, Critical review of analysis and interpretation of nanoindentation test data, Surf. Coat. Technol. 200 (2006) 4153–4165, https://doi.org/10.1016/j.surfcoat.2005.03.018

[33] G.C.A.M. Janssen, M.M. Abdalla, F. van Keulen, B.R. Pujada, B. van Venrooy, Celebrating the 100th anniversary of the Stoney equation for film stress: Developments from polycrystalline steel strips to single crystal silicon wafers, Thin Solid Films 517 (2009) 1858–1867, https://doi.org/10.1016/j.tsf.2008.07.014

[34] G.G. Stoney, The Tension of Metallic Films Deposited by Electrolysis, Proc. R. Soc. A Math. Phys. Eng. Sci. 82 (1909) 172–175. doi:10.1098/rspa.1909.0021.

[35] G. Kresse, J. Furthmüller, Efficient iterative schemes for ab initio total-energy calculations using a plane-wave basis set, Phys. Rev. B - Condens. Matter Mater. Phys. 54 (1996) 11169–11186, https://doi.org/10.1103/PhysRevB.54.11169

[36] G. Kresse, D. Joubert, From ultrasoft pseudopotentials to the projector augmented-wave method, Phys. Rev. B. 59 (1999) 1758–1775, https://doi.org/10.1103/PhysRevB.59.1758

[37] J.P. Perdew, K. Burke, M. Ernzerhof, Generalized gradient approximation made simple, Phys. Rev. Lett. 77 (1996) 3865–3868, https://doi.org/10.1103/PhysRevLett.77.3865

[38] A. Van de Walle, M. Asta, G. Ceder, The alloy theoretic automated toolkit: A user guide, Calphad Comput. Coupling Phase Diagr. Thermochem 26 (2002) 539–553, https://doi.org/10.1016/S0364-5916(02)80006-2

[39] P. Felfer, GitHub - Atom-Probe-Toolbox: Matlab toolbox for APT analysis, (2022). https://github.com/peterfelfer/Atom-Probe-Toolbox (Accessed 19 August 2022).

[40] L. Chen, J. Paulitsch, Y. Du, P.H. Mayrhofer, Thermal stability and oxidation resistance of Ti–Al–N coatings, Surf. Coat. Technol. 206 (2012) 2954–2960, https://doi.org/10.1016/j.surfcoat.2011.12.028

[41] H. Euchner, P.H. Mayrhofer, Vacancy-dependent stability of cubic and wurtzite Ti1−xAlxN, Surf. Coat. Technol. 275 (2015) 214–218, https://doi.org/10.1016/j.surfcoat.2015.05.017

[42] V. Moraes, H. Riedl, C. Fuger, P. Polcik, H. Bolvardi, D. Holec, P.H. Mayrhofer, Ab initio inspired design of ternary boride thin films, Sci. Rep. 8 (2018) 9288, https://doi.org/10.1038/s41598-018-27426-w

[43] P. Villars, H. Okamoto, B-Cr-Si Isothermal Section of Ternary Phase Diagram, (2012). https://materials.springer.com/isp/phase-diagram/docs/c_0977925.

[44] ICDD, Powder Diffraction File - hexagonal CrB2 - 04–004-1734, Powder Diffr. File - Hexag. CrB2 - 04–004-1734. (2011).

[45] ICDD, Powder Diffraction File - cubic Si - 00–027-1402, Powder Diffr. File - Cubic Si - 00–027-1402. (2017).

[46] M.M. Dorri, J. Thörnberg, N. Hellgren, J. Palisaitis, A. Petruhins, F.F. Klimashin, L. Hultman, I. Petrov, P.O.Å. Persson, J. Rosen, Synthesis and characterization of CrB2 thin films grown by DC magnetron sputtering, Scr. Mater. 200 (2021) 113915, https://doi.org/10.1016/j.scriptamat.2021.113915

[47] M. Stüber, H. Riedl, T. Wojcik, S. Ulrich, H. Leiste, P.H. Mayrhofer, Microstructure of Al-containing magnetron sputtered TiB2 thin films, Thin Solid Films 688 (2019) 137361, https://doi.org/10.1016/j.tsf.2019.06.011

[48] P.H. Mayrhofer, C. Mitterer, J.G. Wen, J.E. Greene, I. Petrov, Self-organized nanocolumnar structure in superhard TiB2 thin films, Appl. Phys. Lett. 86 (2005) 1–3, https://doi.org/10.1063/1.1887324

[49] R. Hahn, V. Moraes, A. Limbeck, P. Polcik, P.H. Mayrhofer, H. Euchner, Electron-configuration stabilized (W,Al)B2 solid solutions, Acta Mater. 174 (2019) 398–405, https://doi.org/10.1016/j.actamat.2019.05.056

[50] L. Zauner, R. Hahn, E. Aschauer, T. Wojcik, A. Davydok, O. Hunold, P. Polcik, H. Riedl, Assessing the fracture and fatigue resistance of nanostructured thin films, Acta Mater. 239 (2022) 118260, https://doi.org/10.1016/j.actamat.2022.118260

[51] M. Audronis, A. Leyland, P.J. Kelly, A. Matthews, The effect of pulsed magnetron sputtering on the structure and mechanical properties of CrB2 coatings, Surf. Coat. Technol. 201 (2006) 3970–3976, https://doi.org/10.1016/j.surfcoat.2006.08.006

[52] K.L. Dahm, L.R. Jordan, J. Haase, P.A. Dearnley, Magnetron sputter deposition of chromium diboride coatings, Surf. Coat. Technol. 108–109 (1998) 413–418, https://doi.org/10.1016/S0257-8972(98)00568-4

[53] S. Zhang, Z. Wang, P. Guo, P. Ke, M. Odén, A. Wang, Temperature induced superhard CrB2 coatings with preferred (001) orientation deposited by DC magnetron sputtering technique, Surf. Coat. Technol. 322 (2017) 134–140, https://doi.org/10.1016/j.surfcoat.2017.05.030

[54] C. Fuger, R. Hahn, L. Zauner, T. Wojcik, M. Weiss, A. Limbeck, O. Hunold, P. Polcik, H. Riedl, Anisotropic super-hardness of hexagonal WB2 ± z thin films, Mater. Res. Lett. 10 (2022) 70–77, https://doi.org/10.1080/21663831.2021.2021308

[55] C.L. Jiang, Z.L. Pei, Y.M. Liu, H. Lei, J. Gong, C. Sun, Determination of the thermal properties of AlB 2 -type WB 2, Appl. Surf. Sci. 288 (2014) 324–330, https://doi.org/10.1016/j.apsusc.2013.10.027

[56] CrysTec GmbH, Data sheet: Sapphire for Research and Development, (2022). http://www.crystec.de/daten/al2o3.pdf (Accessed 19 August 2022).

[57] P.V. Kiryukhantsev-Korneev, J.F. Pierson, K.A. Kuptsov, D.V. Shtansky, Hard Cr-Al-Si-B-(N) coatings deposited by reactive and non-reactive magnetron sputtering of CrAlSiB target, Appl. Surf. Sci. 314 (2014) 104–111, https://doi.org/10.1016/j.apsusc.2014.06.160

[58] ICDD, Powder Diffraction File - hexagonal CrSi2 - 04–001-7333, Powder Diffr. File - Hexag. CrSi2 - 04–001-7333. (2011).

[59] ICDD, Powder Diffraction File - rhombohedral Cr2O3 - 00–006-0504, Powder Diffr. File - Rhombohedral Cr2O3 - 00–006-0504. (1970).

[60] ICDD, Powder Diffraction File - orthorhombic CrB - 04–003-6125, Powder Diffr. File - Orthorhombic CrB - 04–003-6125. (2011).

[61] ICDD, Powder Diffraction File - rhombohedral Al2O3 - 00–046-1212, Powder Diffr. File - Rhombohedral Al2O3 - 00–046-1212. (1970).

[62] P.K. Liao, K.E. Spear, The B-Cr (Boron-Chromium) system, Bull. Alloy Phase Diagr. 7 (1986) 232–237, https://doi.org/10.1007/BF02868996

[63] N. Birks, G.H. Meier, F.S. Pettit, Introduction to the high temperature oxidation of metals, Second edition., Cambridge University Press, 2006, https://doi.org/10.1017/CBO9781139163903